Mesoscale porosity at the dentin-enamel junction could affect the biomechanical properties of teeth

Elsa Vennat, Wang Wenlong, R. Genthial, Bertrand David, Elisabeth Dursun, Aurélien Gourrier

To cite this version:

Elsa Vennat, Wang Wenlong, R. Genthial, Bertrand David, Elisabeth Dursun, et al.. Mesoscale porosity at the dentin-enamel junction could affect the biomechanical properties of teeth. Acta Biomaterialia, 2017, 51, pp.418-432. 10.1016/j.actbio.2017.01.052 . hal-01446736

This is a preprint version of the accepted manuscript
Online version: https://www.sciencedirect.com/science/article/pii/S1742706117300612
doi: http://dx.doi.org/10.1016/j.actbio.2017.01.052
Please cite as: Vennat, E., Wang, W., Genthial, R., David, B., Dursun, E. & Gourrier, A. (2017). *Mesoscale porosity at the dentin-enamel junction could affect the biomechanical properties of teeth*, Acta Biomater. 51, 418-432. doi: 10.1016/j.actbio.2017.01.052

Mesoscale porosity at the dentin-enamel junction could affect the biomechanical properties of teeth

Elsa Vennat[a,*], Wenlong Wang[a], Rachel Genthial[b], Bertrand David[a],
Elisabeth Dursun[c,d], Aurélien Gourrier[b,e,*]

[a] MSSMat, CNRS, Centrale-Supélec, Université Paris-Saclay, 92290 Châtenay-Malabry, France
[b] Univ. Grenoble Alpes, LIPHY, F-38000 Grenoble, France
[c] URB2i, Université Paris Descartes, Montrouge, France
[d] Hôpital Albert Chenevier, Créteil, France
[e] CNRS, LIPHY, F-38000 Grenoble, France
[*] Corresponding authors: elsa.vennat@centralesupelec.fr, aurelien.gourrier@univ-grenoble-alpes.fr

Abstract: In this paper, the 3D-morphology of the porosity in dentin is investigated within the first 350 µm from the dentin-enamel junction (DEJ) by fluorescence confocal laser scanning microscopy (CLSM). We found that the porous microstructure exhibits a much more complex geometry than classically described, which may impact our fundamental understanding of the mechanical behavior of teeth and could have practical consequences for dental surgery.

Our 3D observations reveal numerous fine branches stemming from the tubules which may play a role in cellular communication or mechanosensing during the early stages of dentinogenesis. The effect of this highly branched microstructure on the local mechanical properties is investigated by means of numerical simulations. Under simplified assumptions on the surrounding tissue characteristics, we find that the presence of fine branches negatively affects the mechanical properties by creating local stress concentrations. However, this effect is reduced by the presence of peritubular dentin surrounding the tubules.

The porosity was also quantified using the CSLM data and compared to this derived from SEM imaging. A bimodal distribution of channel diameters was found near the DEJ with a mean value of 1.5–2 µm for the tubules and 0.3–0.5 µm for the fine branches which contribute to 30% of the total porosity (~1.2%). A gradient in the branching density was observed from the DEJ towards the pulp, independently of the anatomical location.

Our work constitutes an incentive towards more elaborate multiscale studies of dentin microstructure to better assess the effect of aging and for the design of biomaterials used in dentistry, e.g. to ensure more efficient bonding to dentin. Finally, our analysis of the tubular network structure provides valuable data to improve current numerical models.

Keywords: Confocal laser scanning microscopy (CLSM); Dentin; DEJ; Tubules; Branching; Porosity; 3D-imaging; SEM

1. Introduction

Dentin is a mineralized tissue located between the enamel and the pulp cavity in the tooth that plays an essential role in absorbing and distributing stresses generated by mastication [1]. Such functions are primarily determined by the tissue structure and composition. Dentin is essentially composed of type I collagen fibrils mineralized by hydroxyapatite nanocrystals and exhibits a natural porosity in the form of tubules produced during the dentinogenesis step of tooth formation. This process appears to be strongly directional, whereby odontoblasts, the tissue forming cells, move collectively from the dentino-enamel junction (DEJ) to the pulp [2]. As the extracellular matrix densifies, long slender odontoblasts processes form to maintain cellular contact along the path to the DEJ. The voids, necessary to accommodate the presence of odontoblastic processes, therefore appear as a dense organization of highly anisotropic tubules, radially oriented, with increasing density from the DEJ to the pulp [3]. This growth process also results in a strong tissue texture, with collagen fibrils organized in two preferential orthogonal directions: a minor fraction aligned along the tubules in a thin peritubular collar (<1 μm) and the remaining part lying in the orthogonal direction between tubules [4].

The impact of this microstructure on the mechanical properties has been thoroughly investigated from the macroscopic to the nanoscopic scales [5–11,1]. Those studies concluded to the existence of a zone of ~300 μm below the DEJ which is critical for the mechanical adaptation between the hard enamel and the softer pulp dentin. Important structural changes were reported in this zone in the form of a pronounced collagen disorganization and decrease in mineralization closer to the DEJ [4] and the appearance of microbranches stemming from the tubules towards the DEJ [12]. However, while the gradual changes in tissue structure have clearly been related to the adaptive functional behavior of this interphase, the potential impact of the complex branching morphology on the mechanical properties is unclear.

The microtubule organization has been extensively studied in 2D with increasing resolution levels using transmission brightfield light microscopy [12,13], scanning and transmission electron microscopy (SEM, TEM) [13–15] and atomic force microscopy (AFM) [16,17]. Although not always explicitly stated, a strong assumption supporting those 2D studies lies in the strong degree of co-alignment of the tubules. Thus, following well controlled sample preparation protocols, the tubules can be viewed along their main orientation axis (longitudinal section) or crosswise (transverse sections). Nevertheless, such analysis fails to provide quantitative information concerning out-of-plane details. So far, 3D quantifications of dentinal porosity were carried out using mercury intrusion porosimetry by Vennat et al. (2009) [18], but this procedure only provides average porosity values which cannot be directly related to the microstructure. Recent progress in the field of X-ray tomography making use of the phase contrast [19] and coherence [20] of very bright synchrotron sources has provided sufficient resolution to resolve the tubules in 3D. However, such measurements remain challenging and cannot be performed routinely. Similarly, focused ion beam instruments coupled with SEM (FIB-SEM) constitute an interesting alternative despite the destructive nature of this method [21]. Finally, the progress made in the last two decades in the field of optics, particularly in non-linear imaging, has provided new insight on the tissue-microstructure relationship [22,23]. However, to this day, a precise 3D description and quantification of the tubule network geometry, connectivity and of the corresponding local porosity in the vicinity of the DEJ is still lacking.

In this paper, we investigate the complex tubular branching geometry in a region of ~350 μm from the DEJ using confocal laser scanning microscopy (CLSM). In the field of odontology, CLSM is essentially used to study infiltrated dentin and quantify the penetration depth into enamel [24–27]. Recently, Eltit et al. [28] also used confocal microscopy to image cracks resulting from mechanical testing in 3D. However, this technique has rarely been used to analyze the 3D porous microstructure of dentin at the micron level. This is somewhat surprising since, in comparison to the above mentioned X-ray and electron microscopy methods, CLSM allows large areas to be scanned in a relatively short time, is less destructive, easier to operate and can be accessed at a lower cost.

Our data provide an accurate visualization of the porosity network in 3D, with high spatial resolution over statistically representative sample volumes, which allows re-assessing the porosity in dentin with a higher precision than has been obtained so far. Using those measurements, we provide a geometrical description of the porous structure, introducing new quantitative microstructural parameters to describe the multiscale tubule branching. We show, using simple simulations, that such geometrical characteristics can greatly affect the mechanical properties of the dentinal substrate. This suggests that more realistic microstructures including the geometrical characteristics of the porosity should be used for accurate modeling of tooth biomechanical function.

2. Materials and methods

2.1. Sample preparation

Three non-carious human third molars were used for this study. The teeth were obtained following informed consent according to the protocols approved by the review board of the Dental Faculty of Paris-Descartes University at 4 °C from young donors of 15–20 years. After cutting with a diamond saw (Presi Mecatome T210), the samples were reduced to a thickness of 200 ± 10 μm by polishing on both sides using 4000 grade SiC abrasive papers (Presi, Minitech 233). Our embedding protocol ensures that only the outer surface of the teeth was in contact with the resin to facilitate the cutting (by avoiding direct contact between the tooth and sample holder and allowing more accurate orientation with respect to the saw) and polishing (by fixing the sample on the metallic sample holder by gluing only the surrounding resin with cyanoacrylate glue) steps without obstructing the porosity. The sample sections of S1, S2 and S3 were then stained in glycerol with 0.02 wt% Rhodamine B (RhB) for 48 h at room temperature and mounted between glass slides using the same medium. S1 was used to establish the proof of feasibility of the study and to perform the morphological observation and quantification (Section 3.1). S2 and S3 were used to confirm the findings revealed by the study of S1 and to investigate the porous network variation with location and depth (Section 3.2.2).

2.2. Light microscopy

The samples were first observed by transmission light microscopy (Olympus IX71) with or without cross-polarizers, in order to choose the locations to be imaged.

2.3. Confocal laser scanning microscopy (CLSM)

The polished sections were observed with a motorized inverted confocal laser scanning microscope (SP8, Leica). A 40# oil immersion lens (1.3NA) was used and glycerol was chosen as a good compromise between index matching to minimize the aberrations and artifacts with the objective and efficient mounting medium for the fluorescent die. The RhB was excited at 561 nm and the fluorescence emission was collected between 566 and 636 nm with a hybrid detector. Brightfield transmission images were simultaneously acquired on a second channel using a dedicated photomultiplier. Five locations per sample were imaged at the DEJ: two in the distal and mesial quadrants at the basis of the cervical third of the crown, two in the distal and mesial quadrants in the middle third of the crown (approximately at the axial position of the pulpal horns) and one in the middle of the occlusal third of the crown. For each location, a region of 387.5×387.5 μm^2 in plane and 35 μm in depth was scanned in steps of 189.3 nm laterally and 350 nm axially. The theoretical resolution (in the absence of aberrations) was 230 nm (lateral) and 1.0 μm (axial).

2.4. Scanning electron microscopy (SEM)

To have a comparative reference value for the tubule size and porosity, S1 was observed by SEM using a Helios 660 (FEI) in back-scattered electron (BSE) collection mode to obtain a map of the chemical contrast. The sample (obtained following the protocol described in Section 2.1 and previously observed by CLSM) was dehydrated, then fixed using a conductive silver coating on the sample holder. No other treatment was carried out.

2.5. Image treatment and analysis

Image treatment and analysis were performed with ImageJ software (Rasband, W. S., ImageJ, U.S. National Institutes of Health, http://imagej.nih.gov/ij/).

2.5.1. 3D visualization and morphological analysis

2.5.1.1. 3D vizualization. The stack of images obtained by CLSM were used to visualize the microstructure of the porous media. 3D representations were obtained using ImageJ (Volume Viewer by Barthel K. U. and 3D viewer by Schmid et al. [29]) after binarization.

2.5.1.2. Tubule shape characterization. The image treatment and analysis protocol used in this study is described in Fig. 1. The selected tubule is isolated using the ‘‘crop’’ and ‘‘erosion dilation’’ tools of Image J and the ‘‘Particle Analyser’’ of the Bone J plugin [30]. The shapes of the tubules in the area chosen were analyzed using Image J and the ‘‘Particle Analyser’’ of the Bone J plugin which allows particle counting and characterization. The principal direction of inertia of the selected tubule was deduced and a projection along this axis was performed using the ‘‘Z-project’’ tool.

2.5.1.3. Y-shaped branches. Five Y-shaped branches were isolated and analyzed to derive the skeleton. The treatment consisted in thresholding, filtering and removing numerical artefacts manually. The skeleton was obtained using the Matlab (MathWorks) ‘‘Skeleton3D’’ and ‘‘Skel2Graph3D’’ functions proposed by Kerschnitzki et al. [31] and then analyzed using the ImageJ function ‘‘Analyse Skeleton (2D/3D)’’.

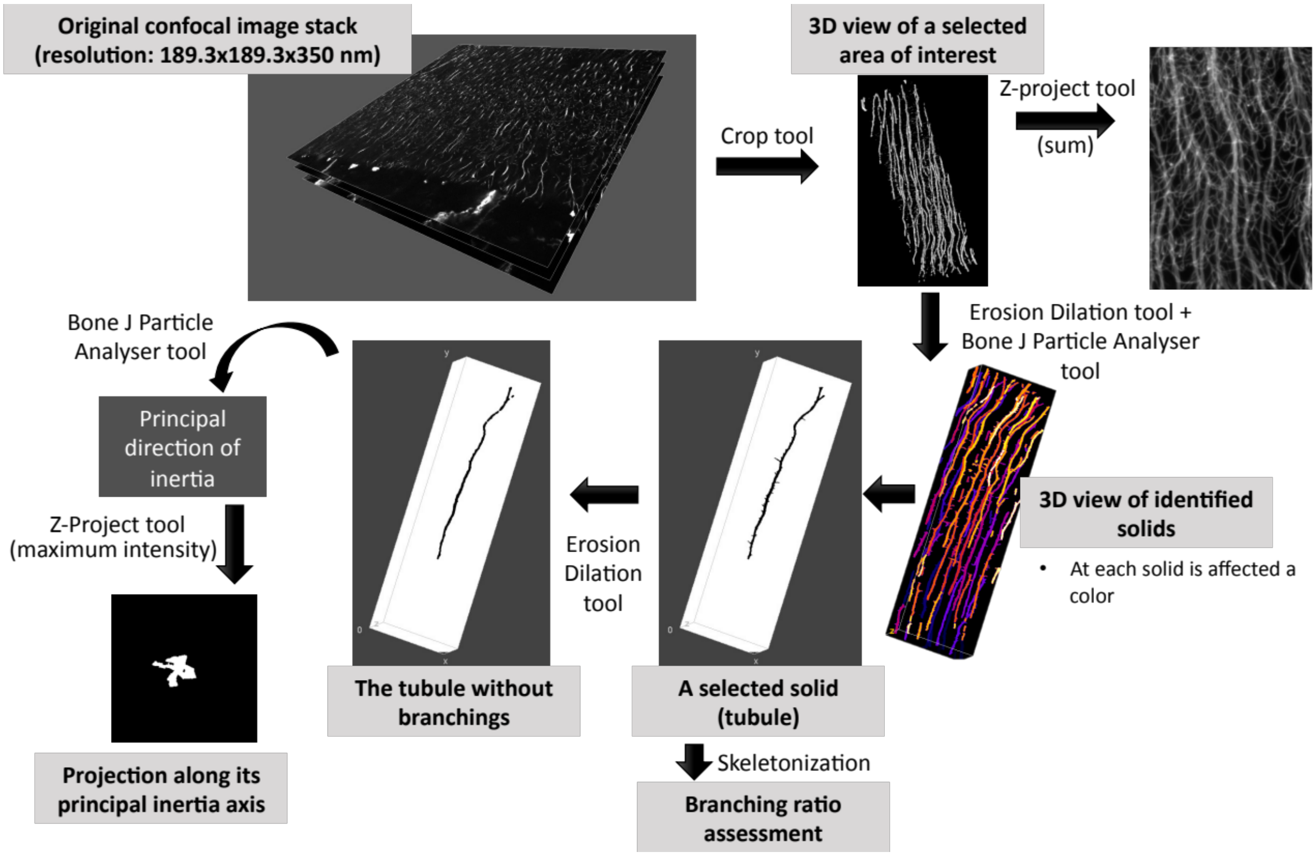

Figure 1. Image treatment and analysis protocol to analyze the tubule shape

2.5.2. Pore size distribution and porosity

2.5.2.1. SEM images analysis. The protocol used to analyze the SEM images is described in Fig. 2. The original SEM images were filtered using a median filter to reduce noise and binarized by thresholding (preserving the tubule’s shape as close as possible as the observed one). The binarized image was analyzed using the ‘‘Analyze Particle’’ tool of ImageJ. The porosity due to the tubules (in white on the binarized SEM image of Fig. 2), the number of tubules (that determines the tubule density) and the minimum Feret’s diameter are obtained.

2.5.1.2. CLSM images analysis. CLSM images analysis. Four binary sets were obtained by thresholding the data to assess the total porosity of the stack. The first two were generated by applying two extreme fixed thresholds

- Threshold 1 (T1) was intentionally low to allow the detection of small porosities.
- Threshold 2 (T2) was intentionally high to see the impact of threshold variation on the results.

The two other sets were obtained using two adaptive thresholding methods:

- Huang’s method (TH) (a method based on minimizing the measures of fuzziness of the input image) [32].
- Li’s method (TL) (a method based on the gray level histogram and incorporating the minimum cross entropy method) [33].

After binarization of the whole image stack obtained by CLSM (a volume of 387.50 × 387.50 × 35 μm^3), a maximal covering sphere (MCS) algorithm was used to determine pore size distribution [34,35]. The local pore size was defined as the diameter of the largest sphere containing the point considered and contained in the pore space. To achieve this the ‘‘Thickness” tool of the Bone J plugin [30] was used.

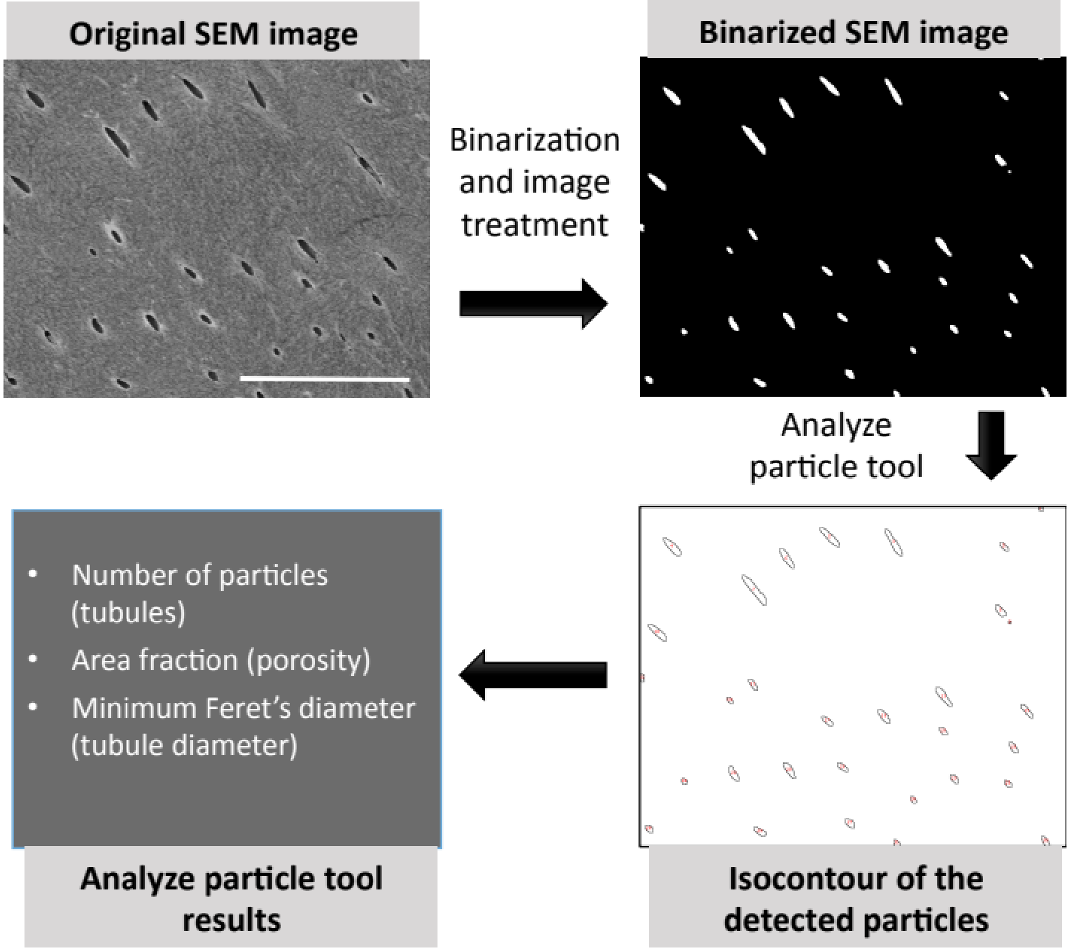

Figure 2. EM image analysis protocol. Scale bar: 30 µm

2.5.3. Statistics

The channel diameters found with the MCS algorithm were analyzed using the Kruskal–Wallis test. The significance level was fixed at p = 0.05.

2.6. Numerical simulations

In order to assess the potential impact of the porous microstructure revealed by CLSM on the mechanical properties of the dentinal tissue, numerical simulations were performed using the Finite Element Method (FEM) using the Comsol Multiphysics software. In particular, the “Structural Mechanics” module was used to solve the stationary, local equilibrium equation (with no volume force):

$$Div\sigma = \vec{0}$$

where σ is the stress tensor and *Div* the divergence operator.

Boundary conditions were set to simulate a compression test on the chosen volume (the geometries inside this volume are presented in the next section, they are all presenting one or two main tubules oriented in the z-direction).

On the upper face perpendicular to the tubule axis, we set:

$$\sigma.\vec{e}_z=-f_s\vec{e}_z$$

where $\vec{e}_z$ is the unitary vector of the z-direction and f_s a boundary load (in MPa).

The external lateral faces are free, so we fixed:

$$\sigma.\vec{n}=\vec{0}$$

where $\vec{n}$ is the external normal unitary vector of the considered face.

On the upper face, perpendicular to the tubule axis, we set a fixed constraint:

$$\vec{u}=\vec{0}$$

The chosen geometries are described in the next sectionsbased on our CLSM observations.

The different materials used in the numerical study were considered to be elastically linear. Their behavior was modeled by the classic Hook's law with the properties indicated in Table 1.

Material	E (Gpa)	ν (-)
Enamel	50	0.3
ITD	20	0.3
PTD	30	0.3

Table 1 : Materials properties. E is the elastic (Young's) modulus and υ is the Poisson's ratio. ITD corresponds to intertubular dentin and PTD to peritubular dentin.

2.6.1 Y-shaped branches at DEJ

At the DEJ, the tubules split into smaller branches called Y-shaped branches. Three types of geometries were studied in order to assess the influence of the branching shape on the mechanical behavior in compression (Figure 3). For the Y-J geometry, three cases were considered: hollow tubes surrounded by intertubular dentin (ITD), tubes completely filled by peritubular dentin (PTD) and surrounded by ITD and tubes surrounded by a PTD collar and ITD.

2.6.2 Fine branch shape

Based on the CLSM observation of the fine branches, three geometries were chosen to assess their influence on the mechanical behavior of dentinal tissue under compression (Figure 4).

The meshes of the different microstructures were obtained in Comsol choosing an element size of type "fine" for all defined geometries.

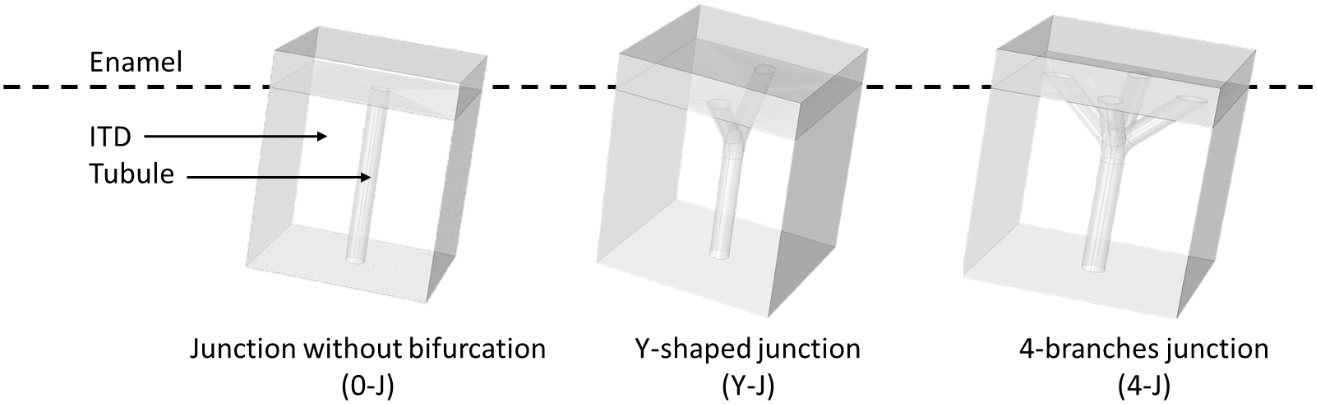

Figure 3. The three geometries (0-J, Y-J and 4-J) considered to assess the influence of the branching shape at the DEJ.

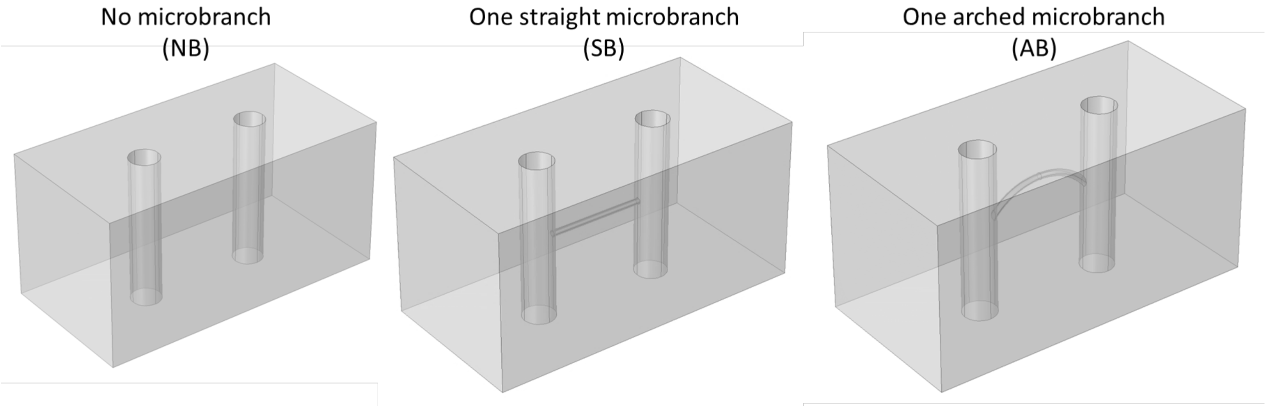

Figure 4. Model used for the simulations with the following three geometries: no branch (NB), straight branch (SB) and arced branch (AB), considered to assess the influence of the branch morphology in the mechanical properties. The solid part is considered as ITD.

3. Results

3.1. Morphological analysis of the porous network

The area studied on the sample S1 is indicated by a red rectangle in Figure 5. It was chosen at the DEJ in the occlusion region which can be identified on the polarized light image as the interface between the enamel exhibiting characteristic birefringence colors and the dentin, shown in gray. In this region, the tubules were found to lie mostly in the X-Y plane, which allowed tracking the tubules over large distances with CLSM.

A qualitative evaluation of the morphology of the medium studied can be performed using 3D visualization of the CLSM data. Figure 6 shows a representative region of the porous structure of the dentin close to DEJ.

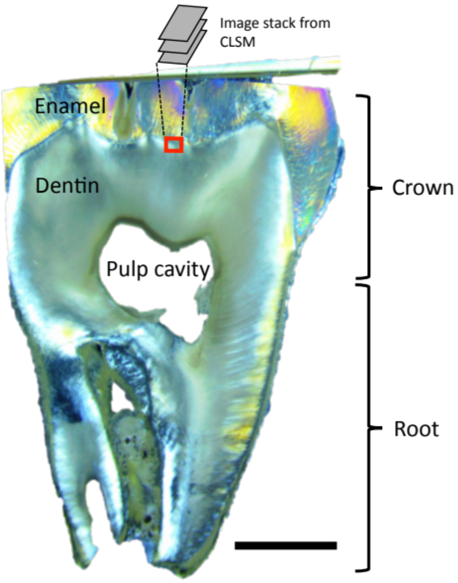

Figure 5. Location of the area selected (in red) on a polarized light microscopy image of an axial section of S1. Scale bar: 3mm.

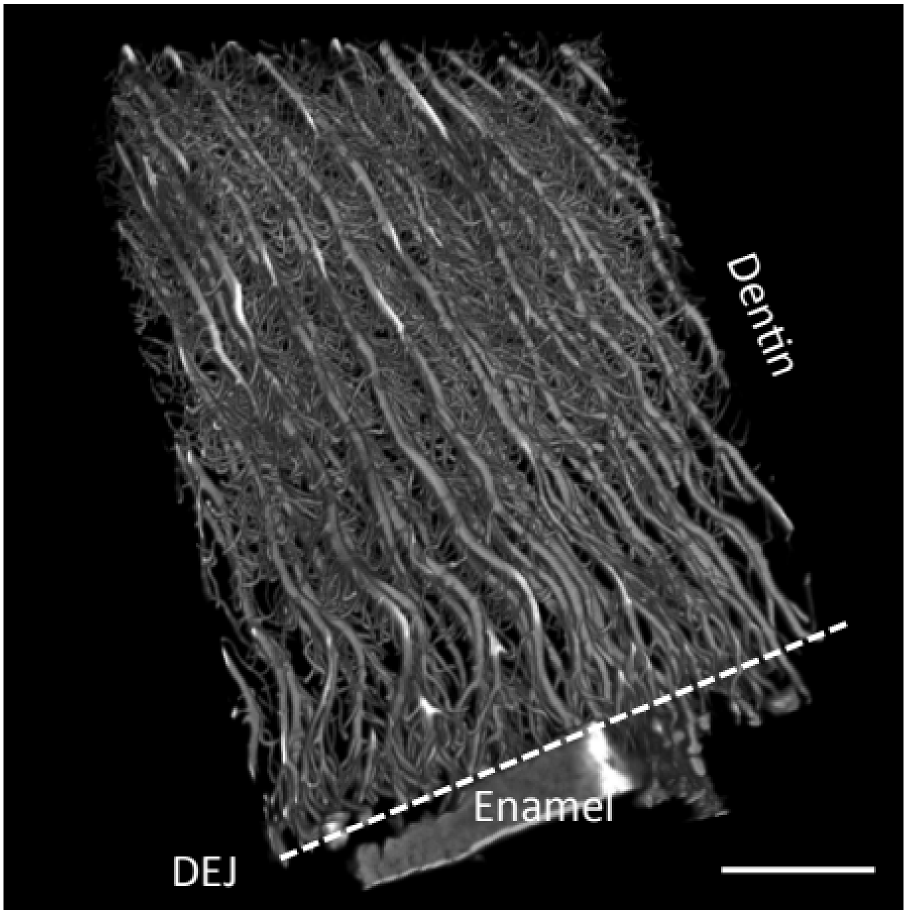

Figure 6. 3D visualization of dentin within 0-120 µm from the DEJ. Scale bar: 30µm.

Clear oscillations of the largest tubules about the principal axis can be observed, which seem more pronounced towards the DEJ. They were described as S-shaped in previous studies [12]. However, this description referred to a 2D observation and it can be assumed that tubules may have a more complex 3D shape than when seen in projection, as in the case of the helicoidal structure recently observed in elephant ivory (Alberic et al. PlosOne, in press [36]). To test this hypothesis, the tubular shape was analyzed following the protocol described in Figure 1. The projections (maximum intensity) of the tubule along the axial direction shown in Figure 7 tend to indicate that the tubular shape is either sinusoidal or helicoidal since the latter implies circular projections.

Figure 7. Examples of tubule projections in the plane perpendicular to the principal axis of inertia (scale bar: 15μm).

The period of these S-shaped tubules lies between 20 and 30 μm and a few tens of lateral branches (fine branches) can be counted along 50 μm of tubule. To better evaluate the degree of branching, we propose to define a branching ratio (BR) which provides a measure of the number of lateral branches by unit length of tubule (μm). The BR is 0.36 branches/μm on average for the dentin tubules of the area chosen.

The S-shaped tubules appear to cross the tissue in phase. A Z-projection was performed by summing slices. The tubules appear to exhibit paths in phase (Figure 8).

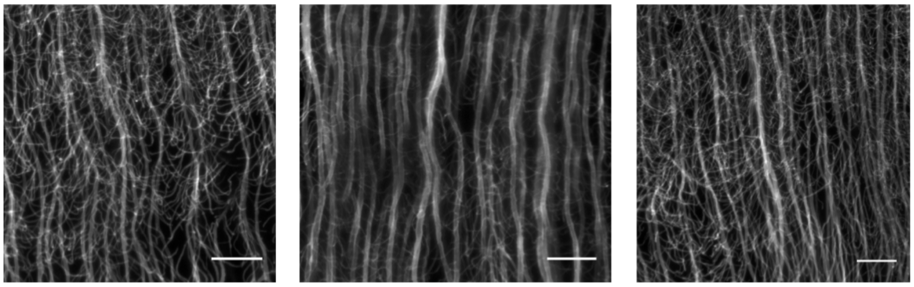

Figure 8. Z-projection (sum) at 3 different distances to the DEJ. Scale bar: 15μm.

Interestingly, the largest tubules can be observed to split between xx-yy μm from the DEJ (Figure 8 middle and left) into two or more branches. In accordance with previous 2D observations, those major branches are termed Y-branches in this paper.

Furthermore, in this sample region, the tubules exhibit a large number of lateral branches (also called fine branches) extending peripherally from the tubule at roughly 45°. This porous network is further illustrated in Figure 9. Generally, these Y-shaped branches exhibit more than two processes which are not found in the same plane. Several of the characteristic morphologies observed are presented in Figure 10.

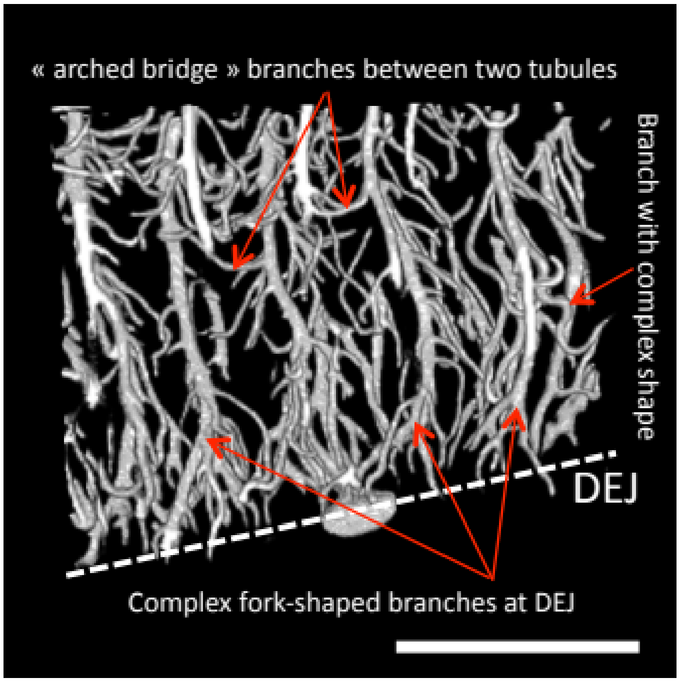

Figure 9. The complex porous network of dentin near the DEJ. Scale bar: 30μm.

Figure 10. Y-shaped branches observed at the DEJ (not represented at the same scale).

A skeleton was derived from those morphologies obtained by thresholding (TL threshold) and then manual cleaning. Figure 11 illustrates a Y-shaped branch and its skeleton. Figure 12 indicates the classification of the branches. As the full length of the terminal branches are not represented by those isolated Y-shaped tubules, they were removed from the analysis. Thus, lateral branches and branches in contact with enamel were not taken into account in the branch length assessment. Table 2 indicates the mean length of the interior branches of the skeleton (in black in Figure 12) and also their minimum and maximum lengths. The branching ratio is also reported.

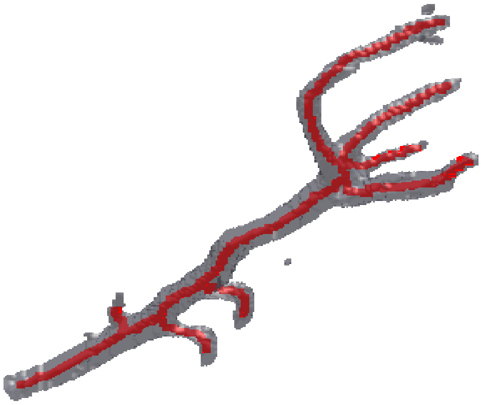

Figure 11. A Y-shaped branch and its skeleton in red.

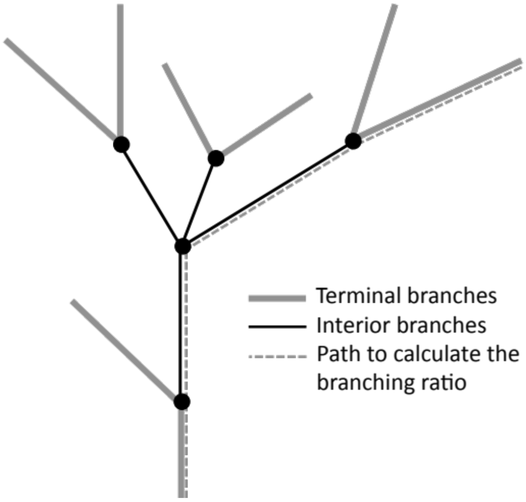

Figure 12. Diagram of the different branches considered in the analysis of the skeleton.

Y-junction name	Mean branch length (µm)	Min branch length (µm)	Max branch length (µm)	BR (branch/µm)
Y1	4.8	0.9	9.4	0.18
Y2	5.9	0.5	18.5	0.10
Y3	3.8	0.5	10.4	0.36
Y4	3.9	0.7	7.2	0.24
Y5	4.2	0.9	7.8	0.36
Mean values (SD)	4.52 (0.9)	0.7 (0.2)	10.7 (4.6)	0.25 (0.11)

Table 2: Analysis of skeleton Y-shaped branches: branch characteristics and branching.

The mean length between two junctions in the Y-shaped branches is around 4.5 µm with a minimum value close to zero (as expected, it is difficult to distinguish between a junction with 4 branches and two close junctions of 3 branches). That is why the branching ratio BR seems a better indicator of the Y-shaped branch morphology. This ratio is 0.25 branches per µm on average (varying from 0.1 to 0.36). It is important to note that this value is obviously an underestimation of the real value because some branches could have been lost during the treatment process.

3.2. Channel diameter distribution (CDD) and porosity assessment

3.2.1 CLSM and SEM assessment for S1

We argue that the principal advantage of CLSM imaging is the three dimensional morphological characterization. However, it is also interesting to investigate the pore structure in terms of porosity and pore size distribution (more specifically CDD in the case of the dentinal tissue). To do so and to validate our results, we first performed a 2D SEM analysis on S1 to obtain a reliable quantification of tubule size at the surface of the sample. The average porosity and pore diameter of S1 were deduced using the protocol presented in Figure 2 on five SEM images in the same dentin area observed by CLSM: the average porosity is 1.2% (±0.2%) and the pore diameter 1μm (±0.2μm). The pore diameter and porosity detected correspond only to the contribution of the tubules. Other types of branching were not taken into account.

Using the protocol defined in 1.5.2.2 on CLSM images of S1, the variation of porosity with depth was determined for each threshold (Figure 13). The mean porosity assessed for each threshold is indicated.

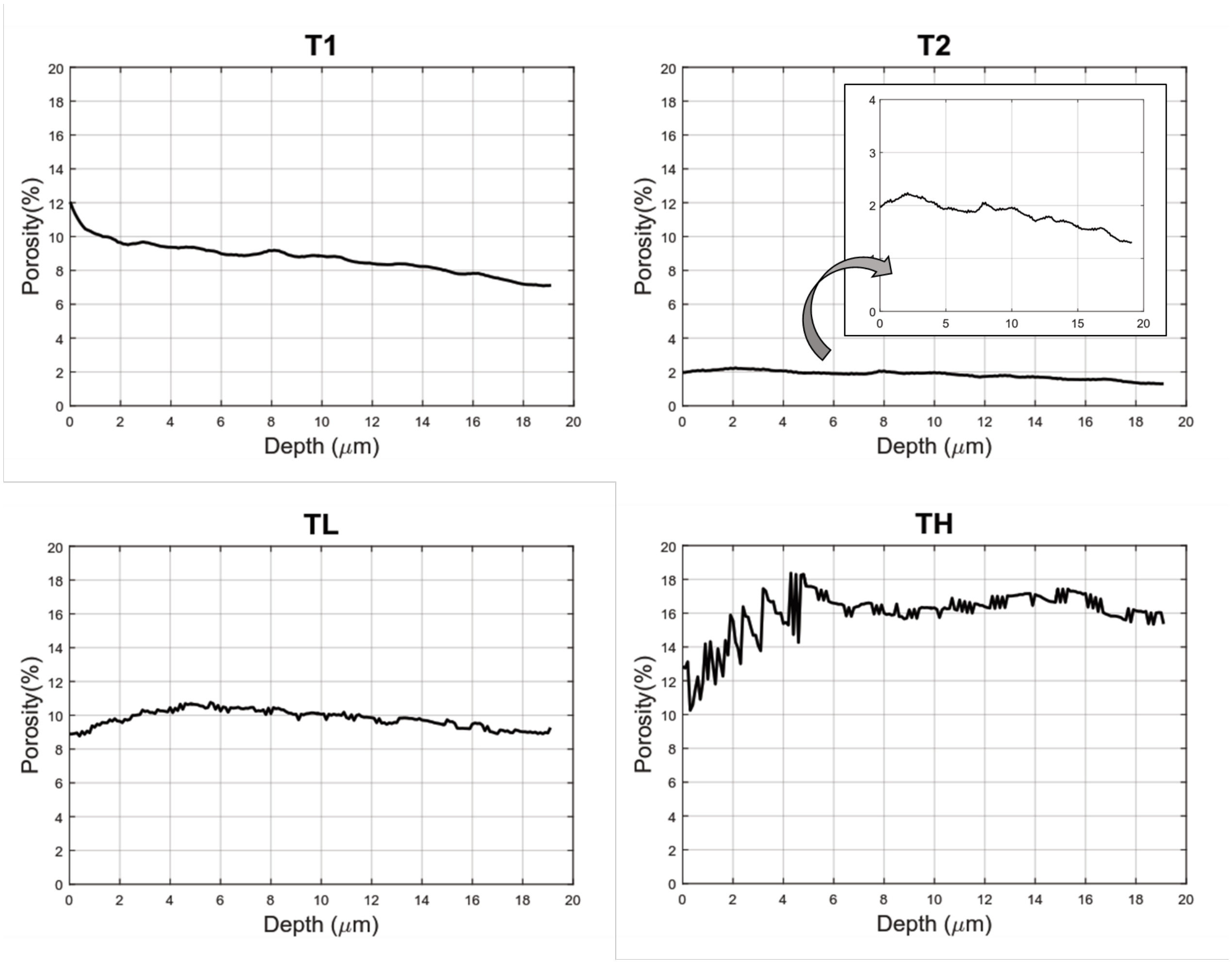

Figure 13. Variation of porosity with depth depending on the chosen thresholding method.

A map of the channel diameters can be obtained for the thresholds chosen using a Maximal Covering Sphere algorithm as explained in section 1.5.2.2.

Figure 14 shows the distribution of the covering diameters (channel diameters). A bimodal distribution was found independently of the chosen thresholding method.

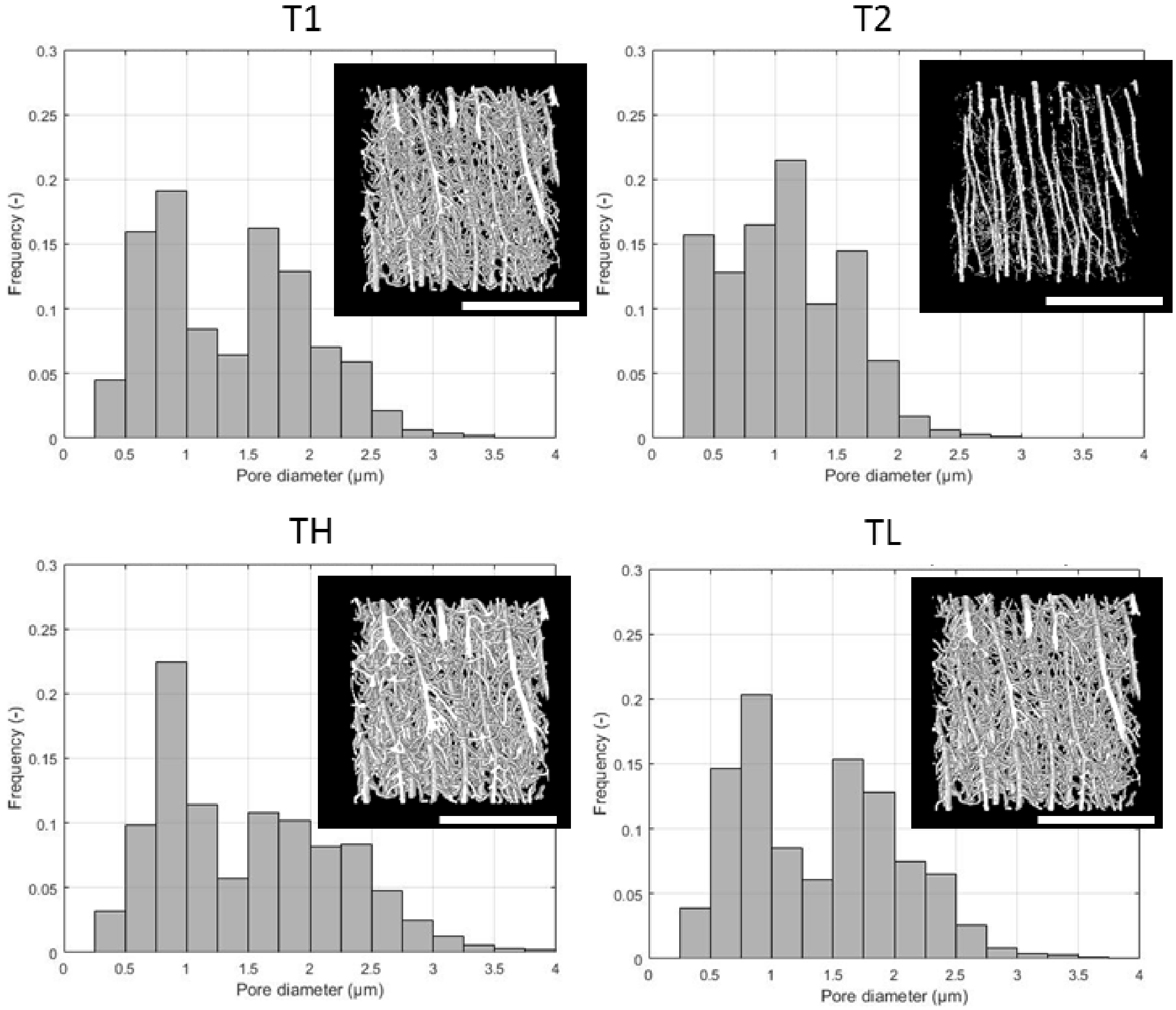
T1

T2

TH

TL

Figure 14. CDD obtained using the MCS algorithm depending on the chosen threshold. The resulting 3D morphology is also illustrated for each thresholding method. Scale bar: 30µm.

The corresponding diameters are illustrated with a 2D covering sphere map on the graph corresponding to TL in Figure 15. This distribution is obviously influenced by the size chosen for the histogram sampling: we chose 250 nm which is consistent with the CLSM acquisition resolution. It is worthwhile noting that a similar analysis conducted with a lower spatial resolution would have produced the same effect as rebinning the histogram of pore diameters shown in Figure 12, i.e. by merging certain channel diameter values making it difficult to clearly distinguish the different types of branches.

This distribution is obviously influenced by the size chosen for the histogram sampling: we chose 250 nm which is consistent with the CLSM acquisition resolution. It is worthwhile noting that a similar analysis conducted with a lower spatial resolution would have produced the same effect as rebinning the histogram of pore diameters shown in Figure 12, i.e. by merging certain channel diameter values making it difficult to clearly distinguish the different types of branches.

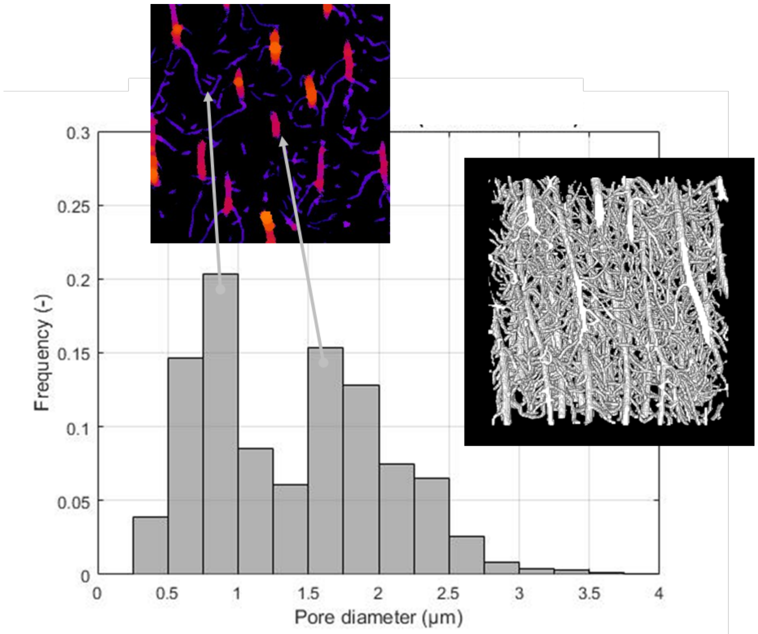

Figure 15. CDD for TL and its corresponding Maximum Covering Sphere Map.

	Location in dentin	**Porosity (SD)**	**Channel size**		
			Microbranches	*Fine branches*	*Tubules and Y-shaped branches*
T1	Near DEJ	8.7 (0.92) %	Not detected	” 0.75µm	” 1.75µm
				Mean diameter: 1.38 µm	
T2	Near DEJ	1.8 (0.24) %	Not detected	” 0.5µm	” 1µm
				Mean diameter: 1.07 µm	
TH	Near DEJ	16.0 (1.42) %	Not detected	” 0.75µm	” 2µm
				Mean diameter: 1.4µm	
TL	Near DEJ	9.8 (0.52) %	Not detected	” 0.75µm	” 1.75µm
				Mean diameter: 1.38µm	
SEM Image analysis	Near DEJ	1.2 (0.2) %	Not detected	Not measured	1 µm
Vennat et al. (2009) [18]	Mean values on massive samples	4%	” 0.6µm (mean value taking into account tubules and other branches)		
Mjör and Nordahl (1996) [12]	Near DEJ		0.025-0.2µm	0.3-0.7µm	0.5-1µm
Pashley (1989) [37]	Near DEJ	1%			0.8µm

Table 3 summarizes the results in terms of porosity and channel size obtained in this study and in the literature.

2.6.2 Variation of the porous structure

In this section, the variation of the channel size distribution with respect to their location in the tooth and also with the distance to the enamel surface is studied using the sample S2 and the threshold TL. Figure 16 illustrates the 5 areas chosen in S2 and their respective CDD. The CDD is clearly bimodal in the five locations (as for S1). The diameters corresponding to the tubules are more frequent in all the selected locations. That is to say that the contribution of the tubules to the total porosity of the selected area is higher than the contribution of fine branches for this sample at the selected locations. Table 4 summarizes the fraction of each pore size to the total porosity depending on their location. The same trends where observed on S3 with less differences of CDD between the areas A1, A2 and A3. For S3, the mean channel diameter is 1.23 (0.01) µm. Channels with a diameter inferior to 1µm constitute 25% of the pore volume and exhibit a mean diameter of 0.50 (0,07) µm. Channels with a diameter superior to 1µm constitute 75% of the pore volume and exhibit a mean diameter of 1.47 (0,01) µm.

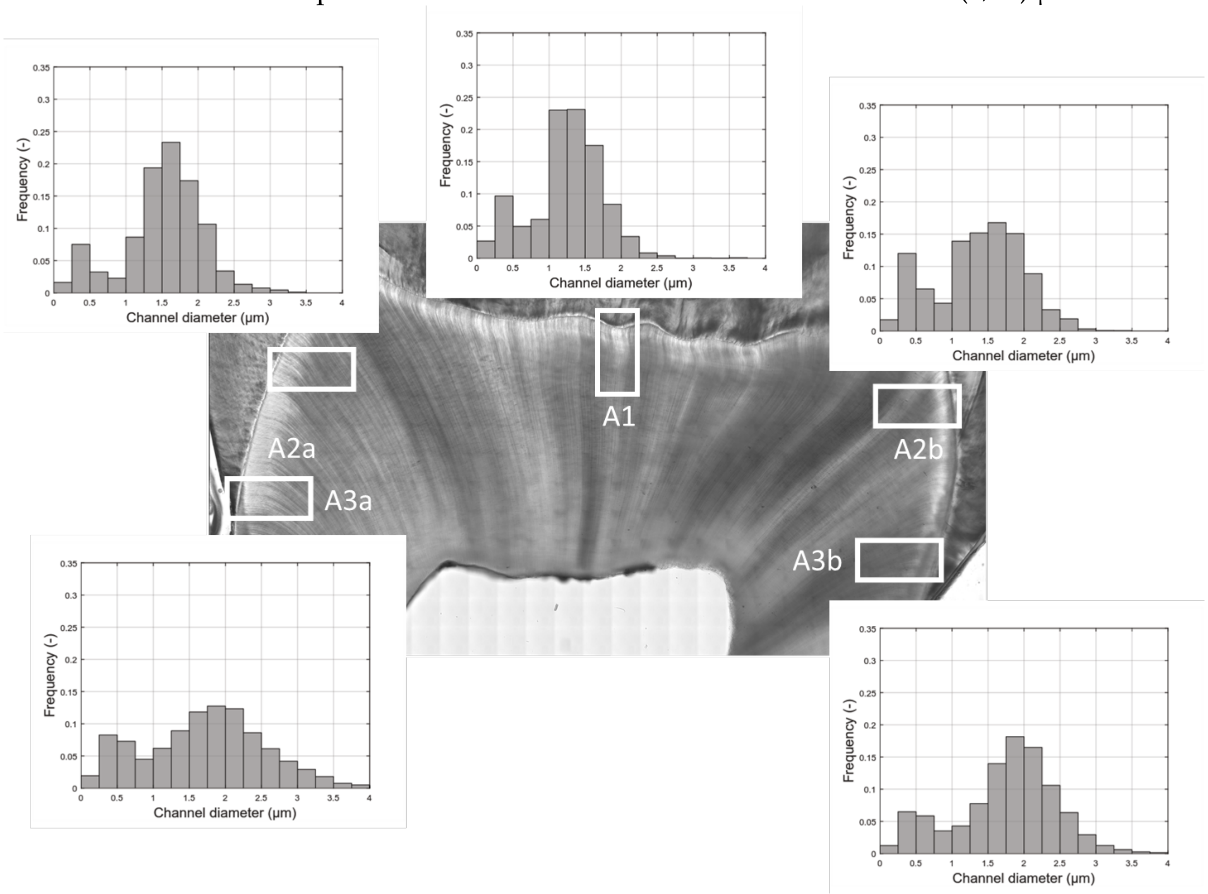

Figure 16: Variation of CDD with location in S2 shown in the background as composite image of the transmission measurements acquired by CSLM (overview scan). Three areas are studied: A1, A2a, A2b, A3A and A3b.

The CDD at the locations A1, A2a, A2b, A3a and A3b in S2 are bimodal with a mean ratio of 24% (of total porosity) due to channels of less than 1µm and 76% due to channels of more than 1µm.

Globally on a volume of roughly 200µm x 200µm x 35µm, the different areas within the dental crown (corresponding to an occlusal area for A1 and for lateral areas for A2a, A2b, A3a and A3b) exhibit similar CDD. However, in all cases, the 3D visualization shows that there is an evolving microstructure from the DEJ towards the pulp.

To confirm and quantify this observation, the variation of CDD with the distance to the DEJ was investigated on the A2b area of S2. Figure 17 illustrates the region studied and defines their locations within this region.

Sample and Area	**Mean channel diameter (SD) in µm**	**Channel diameters ≤ 1 µm**		**Channel diameters > 1 µm**	
		Ratio (%)	Mean diameter (SD) in µm	Ratio (%)	Mean diameter (SD) in µm
S2 A1	1,19 (0,50)	26	0,51 (0,24)	74	1,44 (0,29)
S2 A2a	1,55 (0,55)	15	0,49 (0,21)	85	1,74 (0,37)
S2 A3a	1,72 (0,85)	22	0,56 (0,21)	78	2,1 (0,66)
S2 A2b	1,38 (0,60)	25	0,53 (0,21)	75	1,68 (0,39)
S2 A3b	1,69 (0,68)	17	0,57 (0,21)	83	2,00 (0,47)
Mean values (SD)	1,48 (0,21)	24 (8,5)	0,56 (0,07)	76 (8,5)	1,8 (0,23)
Median values	1,46	23,5	0,54	76,5	1,78

Table 4: Channel diameters depending on location. Two families of channels are distinguished: channels with a diameter superior to one micron and channels with a diameter inferior to one micron. Their part to the total porosity (ratio) is also indicated.

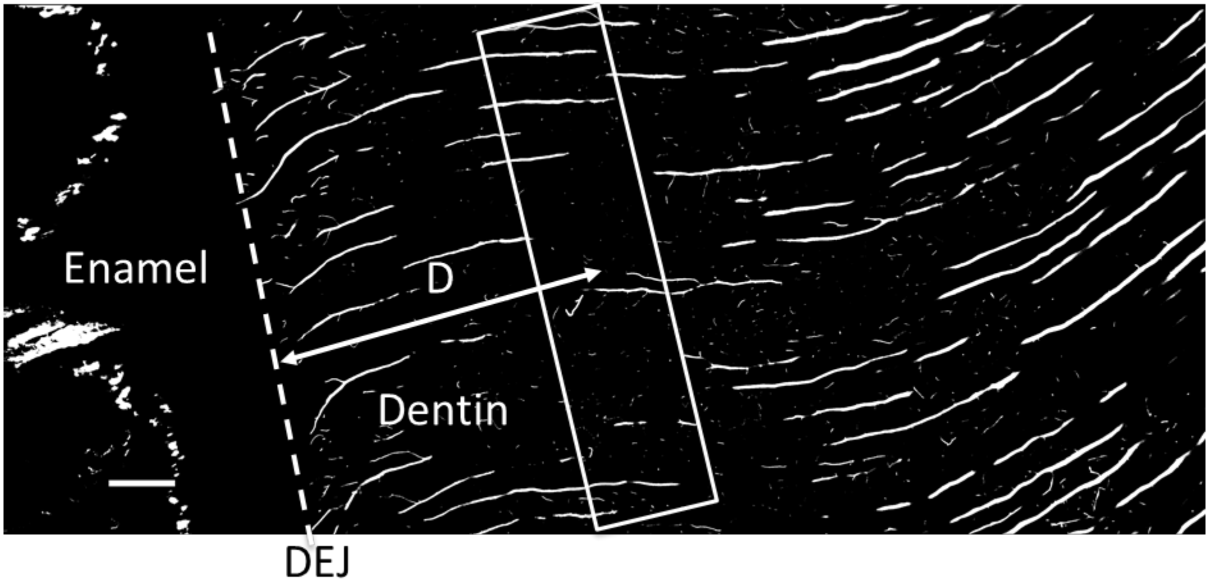

Figure 17: Definition of the locations chosen to study the variation of CDD with distance to DEJ D.

The corresponding CDD histograms are presented in Figure 18.

The CDD clearly exhibits an evolution with distance to the DEJ. Starting from a unimodal distribution around 1µm, the CDD progressively becomes bimodal with two main pore sizes around 0.5µm and 2µm at a distance of 275µm of DEJ.

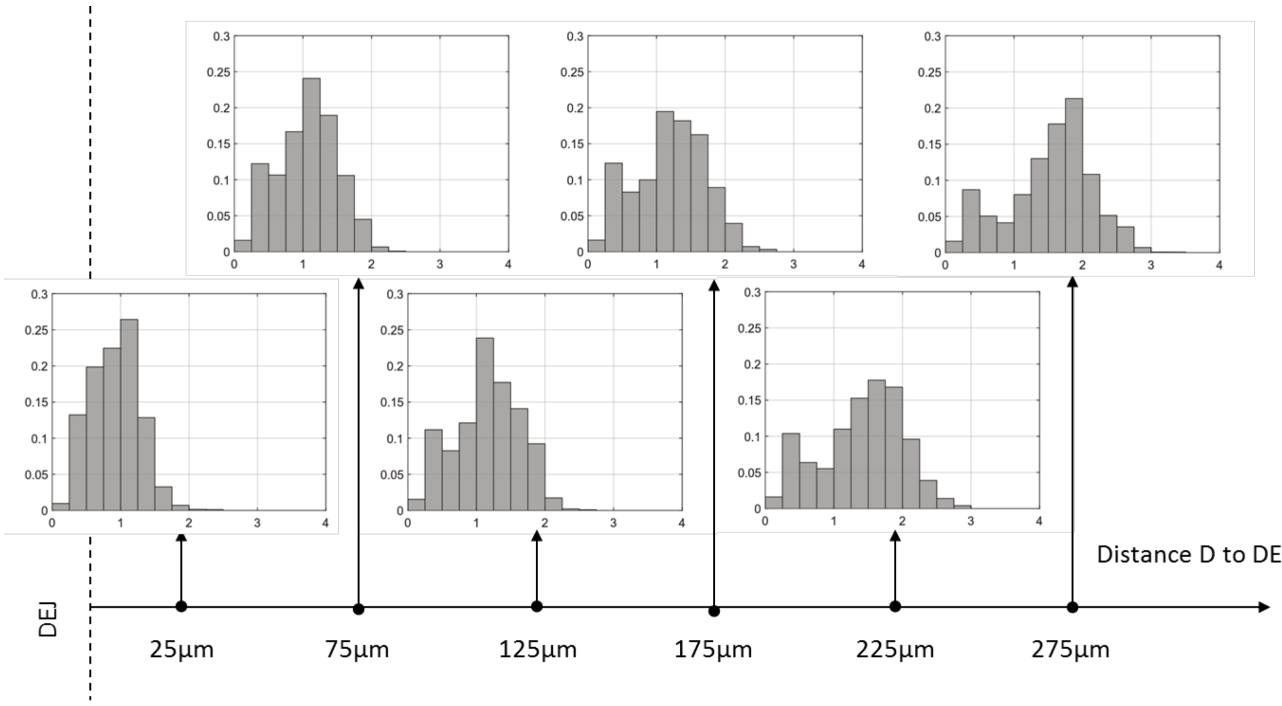

Figure 18 : Variation of CDD with distance to the DEJ D. x-axis and y-axis of CDD histograms are the channel diameter (in µm) and the frequency respectively.

2.6.3 Statistics

In order to test the difference between the CDD with respect to their location in the tooth, the bimodal distributions were split into two unimodal distributions corresponding to tubules (diameter > 1µm) and fine branches (diameter < 1µm). The channel diameters distributions corresponding to each feature (tubule or fine branches) with respect to location (A1, A2a, A2b, A3a, A3d) were not found to be significantly different (p>>0.05). A study on the whole dentin of a sample would fill this gap and highlight the RVE of each part of the dentin bulk.

3.3. Numerical simulations

Based on the results of CLSM images analysis, numerical simulations of the mechanical behavior under compression of the dentinal tissue near the DEJ were carried out.

3.3.1 Terminal branches shape influence

For the three types of geometries 0-J, Y-J an 4-J (and tubules considered as void), the maximal principal stresses in tension (σ_{Imax}) and compression (σ_{IIImax}) were assessed (sufficiently far from the bottom fixed face and from the interface representing the DEJ in order to avoid the influence by the stress concentration generated at those locations)(Table 5). The average displacement in z-direction of the upper face (submitted to the boundary load) was also assessed and is reported in Table 5. In compression, the Y-shaped branches and the 4-branches junctions seem to generate the same order of maximal tensile stress (σ_{Imax}) and the 4-branches junction induces a higher maximal compression stress (σ_{IIImax}) than the two other configurations.

As tubules are known to be surrounded by a peritubular collar, two other configurations of Y-shaped branches have been modeled: one with a tubule full of PTD and another one with a peritubular collar surrounding the tubule and branches. For those configurations, the maps of the first principal stress (which is the principal stress corresponding to tension) and of the third principal stress (which is the principal stress corresponding to compression) in a x-y plane (located at 0.5µm from the DEJ, Figure 19) are shown in Figure 20.

Geometry	**0-J**	**Y-J**	**4-J**
σ_{Imax}	almost zero	$2*f_c$	$1.8*f_c$
σ_{IIImax}	$-f_c$	$-2.4*f_c$	$-6*f_c$
ΔL	ΔL_{0-J}	ΔL_{0-J}	ΔL_{0-J}

Table 5: Results for the three geometries 0-J, Y-J and 4-J in terms of maximal principal stresses and average displacement.

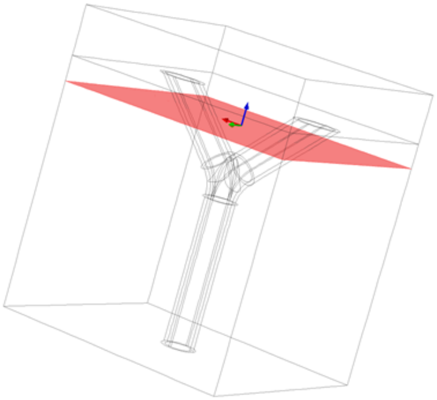

Figure 19 : location of the x-y plane where the stress maps have been represented.

High compression and tension stresses are induced by the presence of hollow tubule and branches. If the tubule and branches are filled with PTD, the stress concentration is reduced. In the most realistic configuration (taking into account hollow tubule surrounded by PTD and ITD) an intermediate behavior is obtained. In this configuration, the maximal stresses seem to be decreased in the PTD region with respect to the case of a sole hollow tube.

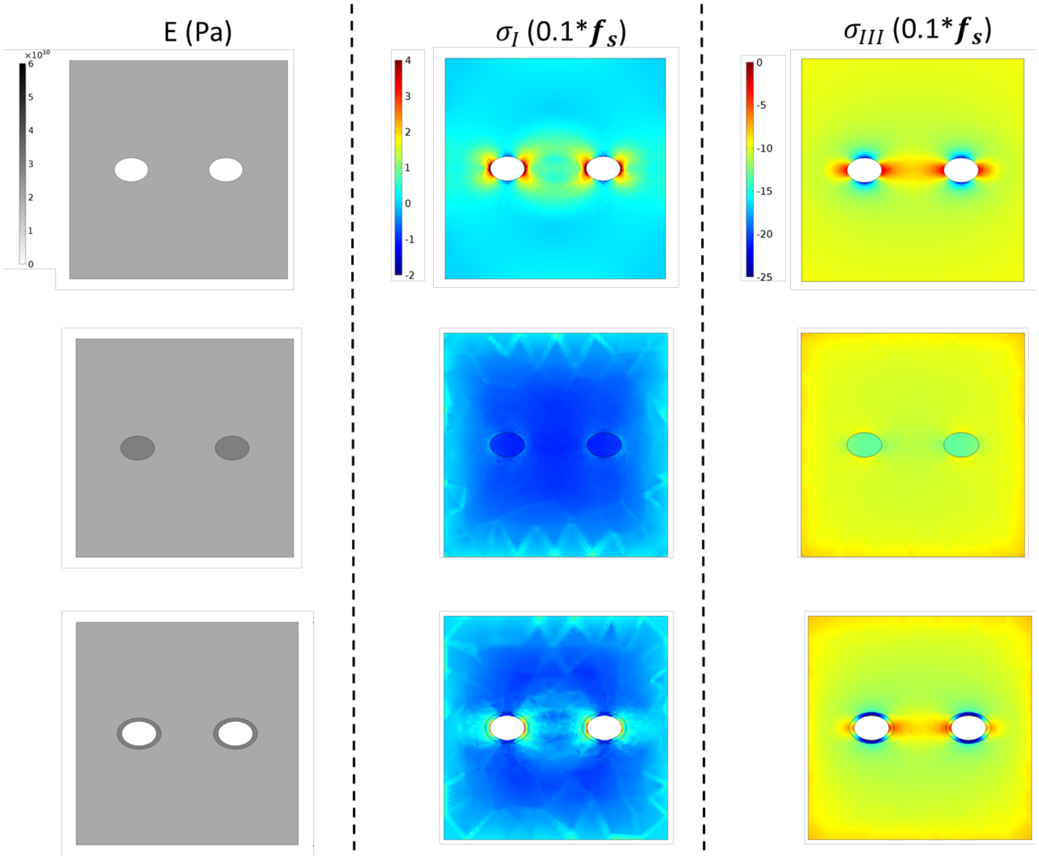

Figure 20: Maps of Young's modulus and of first and third principal stresses in the case of hollow tubes surrounded by ITD (first line), tubes filled by PTD surrounded by ITD, tubes surrounded by a PTD collar and ITD.

3.3.2 Influence of fine branches on the mechanical behavior of dentin

For the three types of geometries NB, SB an AB defined in Figure 4 (and tubules considered as void), the maximal principal stresses in tension (σ_{Imax}) and compression (σ_{IIImax}) were evaluated following the same considerations to avoid the effect of boundaries (Table 6). The average displacement in z-direction of the upper face (submitted to the boundary load) is also reported in Table 6.

Geometry	NB	SB	AB
σ_{Imax}	almost zero	$9*f_s$	$8*f_s$
σ_{IIImax}	$-f_s$	$-5*f_s$	$-3.5*f_s$
ΔL	ΔL_{NB}	ΔL_{NB}	ΔL_{NB}

Table 6: Results for the three geometries NB, SB an AB in terms of maximal principal stresses and average displacement.

As expected, no tensile stress is found in the configuration without branch (NB) whereas the two other configurations give rise to a high tensile stress (almost ten times this applied at the surface load f_s). Similarly, the maximal compressive stress in the NB case is equal to that applied at the surface load f_s

but it is higher in the two other configurations. The presence of branches is, thus, inducing a stress concentration between the branches and the configuration with a straight branch seems the most detrimental. In terms of average displacement induced by the compressive loading, the configurations are equivalent.

4. Discussion

In this paper, the porous structure of dentin within the first 350 μm from the DEJ was investigated at different anatomical locations. The first step was to prove the feasibility of such a study. A first sample (S1) was investigated for this purpose to extract geometric characteristics of the porous network. In addition to the well-known tubules, we thus identified Y-shaped branches mostly forming the end of the tubules towards the enamel surface (also called major branches) and fine branches stemming from the tubules at greater distances from the enamel surface (Figures 6, 8, 9). So far, those channels have been mainly studied in 2D and our 3D CLSM investigation brings new insight into the dentinal porous media near the DEJ. Sinusoidal oscillations of the largest tubules were observed as reported in in previous studies [12] where they were reported as S-shaped. However, this description was established on the basis of 2D observations, which only provides a projection view of a potentially more complex 3D geometry, as in the case of the helicoidal structure recently observed in elephant ivory (Albéric et al. PlosOne, in press [36]). Our study tends to indicate that the tubular shape is either sinusoidal or helicoidal (Figure 7). Therefore, the "S-shaped" description by Mjor [12] derived from 2D analysis seems only partially valid in view of our 3D measurements. Furthermore, the tubules appear to exhibit paths in phase. At the DEJ, the tubules split into Y-shaped branches that should probably be renamed "fork-shaped" branches or "delta-shaped" branches as the major branches observed in 3D generally possess more than two branches which are usually not in the same plane (Figure 10). This should have a strong mechanical consequence because a Y-shaped morphology will lead to a different mechanical behavior than a delta-shaped (with multiple branches) morphology.

The high degree of regularity of the dentinal porous structure revealed by the oscillations of the major branches and the dense branching ratio are quite striking. In particular, the fact that those oscillations appear relatively in phase between different tubules suggests a collective cellular displacement during dentinogenesis. There are indications in the literature that such microstructures could have a beneficial impact on the macroscopic mechanical properties [38,[39]. However, it is unclear whether the stress undergone by the cells during the formation of the extracellular matrix forming the tissue is, in turn, responsible for this collective oscillatory motion. Also intriguing is the observation of the smaller lateral branches which function is not clear. Some are observed to form bridges (arches) between neighboring tubules, which, in addition to a mechanical effect, could indicates potential inter-cellular communication, thus reinforcing the idea of coordinated cell motion. Others form branches which do not connect to other tubules. This could be an artefact of our measurement, due to a lack of spatial resolution to visualize smaller branches that may exist. On the other hand, this considerable degree of branching in the DEJ, where the tubule density is reduced compared to this in the pulp region, was not observed at greater distances from the DEJ and could be due to the need to sense stress or strain and establish cellular communication at the onset of collective cellular motion, i.e. in the first stages of dentinogenesis. Moreover, it is important to point out the fact that this porous network is known to evolve over time, with a progressive filling of the tubules by peritubular dentin [40].

Hence, from a mechanical point of view, the situation can either be described as a complex, multiscale, geometrical organization of pores in a dense tissue or, at the other extreme, of a composite material where the minor volume fraction of peritubular dentin would exhibit the same geometrical organization as the tubules. Added to this, a third case must be considered, this of tubules partly filled by a peritubular collar.

To obtain a first clue on the potential impact of the observed porous microstructure on the mechanical behavior of dentin near the DEJ, simple numerical simulations were performed. The aim of those simulations is clearly not to provide an accurate model of the deformation, but rather to test three different model terminal pore morphologies derived from the CSLM observations, independently of the effect of tissue structure and composition. In compression, with hollow channels surrounded by intertubular dentin, the mechanical behavior of a structure with Y-shaped branches and the geometry with a 4-branches junction is quite equivalent (Table 5). There is a slight increase of stress in the intertubular dentin with a 4-branches junction which is logical because the stress is distributed on a smaller area than in the case of a Y-junction. Here, the question of the role of the peritubular cuff (not observed by CSLM, but clearly visible in backscattered SEM Figure 2, top), which exhibits a higher mineral density than the intertubular dentin arises: should the dentinal channels be considered as a structural reinforcement or as weak points in the material ?

Our first simulations of hollow tubules and branches in homogeneous dentin considered as ITD only (Figure 20, top) reveal a concentration of tensile and compressive stresses during compression loading, which could be at the onset of fracture propagation and, thus, point to a local weakening of the structure. At the other end, when the tubule and branches are occluded by peritubular dentin (Figure 20, middle), less stress concentration is generated. Compared to occluded channels, the case of hollow channels with a peritubular collar in an intertubular dentin matrix exhibits an intermediate behavior (Figure 20, bottom). In this case, the peritubular cuff seems to prevent excessive stress concentration in the intertubular matrix, thus reinforcing the structure.

Only a limited number of studies have experimentally or numerically investigated dentin at such local scale. Despite of their simplicity, our simulations suggest that the stress concentration and distribution is not only determined by the matrix stiffness, but also by the branching geometry and density. This aspect would need to be further investigated since old dentin is known to exhibit a macroscopic fragile behavior compared to younger dentin [41,42]. It would, in particular, be interesting to better understand the role of the peritubular cuff around the tubules and the lateral branches. Moreover, since it is well known that dentin exhibits graded mechanical properties from the DEJ to the pulp, a better understanding of the 3D organization of the dentinal mineral and organic structure at a lower scale in relation to the porous microstructure is needed to reach a comprehensive view of the dentinal tissue behavior.

As a complex secondary porous network of branches linking tubules together was observed in 3D, new geometrical descriptive parameters were proposed. The focus was put on the number of branches per μm of tubular length, the so-called branching ratio (BR) and on the tubular length in between two lateral branches, called branch length. The branching ratio was found to be 0.25 branches per μm on average, with a minimum branch length close to 0 μm (two lateral branches can arise from the same tubule and go in different directions from the same location) and a maximum value of 0.36 μm. This shows that, in the analyzed dentinal region (close to DEJ), there are numerous branches and their number can be assessed and used in a numerical model.

The visualization of the branches shows that they seem arched more than straight, so to assess the impact of such branches, three types of geometries were proposed and numerically submitted to compression loading (Figure 4). The presence of both types of branches generates a stress concentration (both tensile and compressive) but the configuration with a straight branch seems the most detrimental (induces a higher stress concentration). Also, if the channels are seen as a reinforcement (when filled), the arched channel bridging two tubules will have a better mechanical behavior than the straight channel. It is indeed well known (especially in the Civil Engineering field) that an arched geometry enables reaching a longer span by taking advantage of the harmonious stress distribution compared to a straight-line geometry.

A study of the channel diameter distribution and the corresponding porosities was also carried out. The tricky step to perform such analysis is the binarization of the image stack. Four thresholding methods (T1, T2, TH and TL) were chosen and compared in terms of pore size distribution (which we called Channel Diameter Distribution CDD) and total porosity (Figure 14). Characteristic channel diameters corresponding to tubules, Y-shaped branches and fine branches were detected and a bimodal distribution was found (Figures 14, 15, 16) corresponding to tubules and lateral branches (mainly fine branches). The Y-shaped branches location being limited to roughly a few tens of microns from the DEJ, we argue that their contribution is negligible in the CDD we obtained on a larger area. Furthermore, the spatial resolution of CLSM does not allow detecting smaller microbranches and nanoporosities. A FIB-SEM complementary study could be carried out to detect those porosities but, due to the high resolution needed, it will be restricted to smaller volumes than those accessible using CLSM. T1 and TL seem to better preserve the morphological features whereas T2 leads to a loss of information on the lateral branches and TH leads to a melting of geometrical features by overestimating their sizes (the pores types are less distinguishable). The different distributions obtained by T1 and T2 were expected: by using a threshold enabling the preservation of greater details (T1), the dimensions of the porous structure were overestimated; however, all the structures detected were kept. Using T2, the fine branches were not completely observed since they were no longer continuous. Nevertheless, the porosity estimation using this threshold was more realistic. The pore size and porosity values are clearly overestimated for the thresholding methods T1, TH and TL and to a lesser degree for T2. Clearly, such determination of porosity at the limit of the achievable spatial resolution by CSLM is questionable due to improper optical sampling. However, the porosity of 1.8% assessed using T2, which is mainly due to the tubules, agrees with the SEM image analysis carried out on the same sample (1.2%) and those indicated in the literature [18,37]. Thus, it is possible to obtain insight into the tridimensional pore size distribution of dentin using CLSM combined with SEM imaging (CLSM image analysis leading to the CDD and SEM image analysis to a realistic tubule diameter assessment). In Table 7, an estimation of realistic channel diameter distribution combining results from CLSM and SEM is proposed.

Sample and Technique	Mean channel diameter in µm	Fine branches		Tubules	
		Ratio (%)	Mean diameter in µm	Ratio (%)	Mean diameter in µm
S1 CLSM T2	1,07	-	-	-	1,07
S1 CLSM TL	1,38	39	0,68	61	1,82
S1 SEM study	1	-		-	1
S1 combination		39	0,37	61	1

Table 7: Proposition of realistic channel diameter distribution combining results from CLSM and SEM.

From the results obtained for TL, it is interesting to remark that the pore size corresponding to the fine branches represents more than 30% of the pore volume. Thus, although the diameter of the fine branches is small, this pore size is non-negligible due to its high density and must be considered in the porosity assessment and in a numerical model. The variation of the CDD with location within the tooth and according to the distance to the DEJ was also investigated in the two other teeth. As discussed previously, the channel sizes are overestimated but their distribution is realistic and can be compared as a function of location. The variation of the porous structure near the DEJ depending on the location (occlusal or cervical region for example) is not obvious visually, which is confirmed by the statistical analysis (no significant difference of channel diameter distribution at the considered locations was found).

The variation within a same tooth at the same location of CDD with the distance to DEJ was also studied. Here, the distribution is clearly evolving from a unimodal distribution to a bimodal one showing that the tubules and Y-shaped branches have similar diameters in an area close to DEJ (so are included in the same peak of the distribution). When moving away from the DEJ, the tubule diameter becomes larger and lateral branches (with a distinct diameter distribution) appear. At present, only a limited amount of information exists concerning such distribution. It could, therefore, be interesting to further study such a variations throughout the whole dentin (from DEJ to the pulp cavity) to better evaluate the local porous structure of dentin that is too often oversimplified. A local knowledge of dentin structure is indeed crucial to adapt the dental surgery procedures to the location of the lesion. Furthermore, knowing the structural and properties gradient will help understanding the macroscopic mechanical behavior of dentin and could also lead to develop smart biomimetic dental biomaterials that aim to reproduce the relevant properties of the biological tissue.

The porous network revealed in this study could also be used to perform useful numerical simulations of fluid mechanics. It is known that the microstructure and permeability of the tubular system (the complex porous network illustrated here) plays a biological role in nutrient transport [43] and strain sensing. The experimental measurement of dentin permeability is not an easy task and is usually done on massive samples [44]. The data obtained by CLSM could permit building a local geometrical model and assessing local permeability at different locations in the dentin, thereby revealing the property gradients in dentinal tissue.

5. Conclusion

In this paper, we characterized the 3D porous architecture of the dentinal substrate within the first 350 µm from the DEJ using CSLM. The 3D visualization showed that the tubules close to the DEJ split into what appear to be "delta-shaped" junctions. Numerous lateral branches linking the tubules were also observed and quantified. A bimodal distribution of channel diameters was highlighted in this area and the fine branches were found to account for a non-negligible fraction (30 %) of the total porosity in that area. The variation of channel diameter distribution was not significant when changing the anatomical location along the DEJ. Nevertheless, for a given location, an evolving distribution of porosity size was highlighted, showing that microstructural gradients are occurring when moving away from the DEJ. Finally, tThe impact of such microstructures on the local mechanical behavior of the tissue was investigated by means of finite element simulations. We found that, for a given set of tissue characteristics, the existence of microbranches could induce a local stress concentration that may be detrimental for the tooth. We also noticed that this effect could be balanced or even hindered by the presence of a peritubular cuff with increased stiffness. This study therefore emphasizes the importance of the porous microstructure in the vicinity of the DEJ. Because this region is of great importance for the global macroscopic mechanical function of the tooth, more realistic modeling should be performed, including both the graded materials properties evidenced by other authors as well as the porous architecture, including the lowest scales of porosity.

6. Acknowledgments

This work benefited from the financial support of the LabeX LaSIPS (ANR-10-LABX-0040-LaSIPS) managed by the French National Research Agency under the "Investissements d'avenir" program (n°ANR-11-IDEX-0003-02) and the ANR-11-LABX-0030 (LabEx Tec 21).

7. Conflicts of Interest

The authors declare no conflict of interest.

8. References

[1] R.Z. Wang, S. Weiner, Strain-structure relations in human teeth using moiré fringes, J. Biomech. 31 (2) (1997) 135–141.

[2] A. Linde, M. Goldberg, Dentinogenesis, Crit. Rev. Oral Biol. Med. 4 (5) (1993) 679–728.

[3] G.W.J. Marshall, S.J. Marshall, J.H. Kinney, M. Balooch, The dentin substrate: structure and properties related to bonding, J. Dent. 25 (6) (1997) 441–458.

[4] P. Zaslansky, A.A. Friesem, S. Weiner, Structure and mechanical properties of the soft zone separating bulk dentin and enamel in crowns of human teeth: insight into tooth function, J. Struct. Biol. 153 (2) (2006) 188–199.

[5] H. Ryou, N. Amin, A. Ross, N. Eidelman, D. Wang, E. Romberg, D. Arola, Contributions of microstructure and chemical composition to the mechanical properties of dentin, J. Mater. Sci. - Mater. Med. 22 (2011) 1127–1135.

[6] Y.L. Chan, A.H.W. Ngan, N.M. King, Nano-scale structure and mechanical properties of the human dentine-enamel junction, J. Mech. Behav. Biomed. Mater. 4 (5) (2011) 785–795.

[7] R.K. Nalla, J.H. Kinney, R.O. Ritchie, Effect of orientation on the in vitro fracture toughness of dentin: the role of toughening mechanisms, Biomaterials 24 (22) (2003) 3955–3968.

[8] W. Tesch, N. Eidelman, P. Roschger, F. Goldenberg, K. Klaushofer, P. Fratzl, Graded microstructure and mechanical properties of human crown dentin, Calcif. Tissue Int. 69 (2001) 147–157.

[9] R. Craig, F. Peyton, The microhardness of enamel and dentin, J. Dent. Res. 37 (4) (1958) 661–668.

[10] S. Habelitz, S.J. Marshall, G.W. Marshall, M. Balooch, The functional width of the dentino-enamel junction determined by AFM-Based nanoscratching, J. Struct. Biol. 135 (3) (2001) 294–301.

[11] J.D. Wood, R. Wang, S. Weiner, D.H. Pashley, Mapping of tooth deformation caused by moisture change using moiré interferometry, Dent. Mater. 19 (3) (2003) 159–166.

[12] I.A. Mjör, I. Nordahl, The density and branching of dentinal tubules in human teeth, Arch. Oral Biol. 41 (5) (1996) 401–412.

[13] I.A. Mjör, O. Fejerskov, Histology of the Human Tooth, Munksgaard, 1979.

[14] L.E. Bertassoni, K. Stankoska, M.V. Swain, Insights into the structure and composition of the peritubular dentin organic matrix and the lamina limitans, Micron 43 (2–3) (2012) 229–236.

[15] R.K. Nalla, A.E. Porter, C. Daraio, A.M. Minor, V. Radmilovic, E.A. Stach, A.P. Tomsia, R.O. Ritchie, Ultrastructural examination of dentin using focused ion-beam cross-sectioning and transmission electron microscopy, Micron 36 (7–8) (2005) 672–680.

[16] G.W. Marshall, M. Balooch, R.R. Gallagher, S.A. Gansky, S.J. Marshall, Mechanical properties of the dentinoenamel junction: AFM studies of nanohardness, elastic modulus, and fracture, J. Biomed. Mater. Res. 54 (1) (2001) 87–95.

[17] G. Balooch, G.W. Marshall, S.J. Marshall, O.L. Warren, S.A.S. Asif, M. Balooch, Evaluation of a new modulus mapping technique to investigate microstructural features of human teeth, J. Biomech. 37 (8) (2004) 1223–1232.

[18] E. Vennat, C. Bogicevic, J.-M. Fleureau, M. Degrange, Demineralized dentin 3d porosity and pore size distribution using mercury porosimetry, Dent. Mater. 25 (6) (2009) 729–735.

[19] P. Zaslansky, S. Zabler, P. Fratzl, 3D variations in human crown dentin tubule orientation: a phase-contrast microtomography study, Dent. Mater. 26 (1) (2010) e1–e10.

[20] I. Zanette, B. Enders, M. Dierolf, P. Thibault, R. Gradl, A. Diaz, M. Guizar-Sicairos, A. Menzel, F. Pfeiffer, P. Zaslansky, Ptychographic X-ray nanotomography quantifies mineral distributions in human dentine, Sci. Rep. (2015).

[21] J. Earl, R. Leary, J. Perrin, R. Brydson, J. Harrington, K. Markowitz, S. Milne, Characterization of dentine structure in three dimensions using fib-sem, J. Microsc. 240 (1) (2010) 1–5.

[22] R. Elbaum, E. Tal, A.I. Perets, D. Oron, D. Ziskind, Y. Silberberg, H.D. Wagner, Dentin micro-architecture using harmonic generation microscopy, J. Dent. 35 (2) (2007) 150–155.

[23] T. Cloitre, I.V. Panayotov, H. Tassery, C. Gergely, B. Levallois, F.J.G. Cuisinier, Multiphoton imaging of the dentine-enamel junction, J. Biophotonics 6 (4) (2013) 330–337.

[24] H. Meyer-Lueckel, S. Paris, J. Mueller, H. Cölfen, A.M. Kielbassa, Influence of the application time on the penetration of different dental adhesives and a fissure sealant into artificial subsurface lesions in bovine enamel, Dent. Mater. 22 (1) (2006) 22–28.

[25] T. Aguiar, C. Andre, C. Arrais, A. Bedran-Russo, M. Giannini, Micromorphology of resin-dentin interfaces using self-adhesive and conventional resin cements: a confocal laser and scanning electron microscope analysis,

Int. J. Adhes. Adhes. 38 (2012) 69–74.

[26] S. Sauro, R. Osorio, T.F. Watson, M. Toledano, Assessment of the quality of resin-dentin bonded interfaces: an afm nano-indentation, ltbs and confocal ultramorphology study, Dent. Mater. 28 (6) (2012) 622–631.

[27] A. Profeta, F. Mannocci, R. Foxton, T. Watson, V. Feitosa, B. De Carlo, R. Mongiorgi, G. Valdré, S. Sauro, Experimental etch-and-rinse adhesives doped with bioactive calcium silicate-based micro-fillers to generate therapeutic resin-dentin interfaces, Dent. Mater. 29 (7) (2013) 729–741.

[28] F. Eltit, V. Ebacher, R. Wang, Inelastic deformation and microcracking process in human dentin, J. Struct. Biol. 183 (2) (2013) 141–148.

[29] B. Schmid, J. Schindelin, A. Cardona, M. Longair, M. Heisenberg, A high-level 3d visualization api for java and imagej, BMC Bioinformatics 11 (1) (2010) 1.

[30] M. Doube, M. Kłosowski, I. Arganda-Carreras, F.P. Cordelières, R.P. Dougherty, J. S. Jackson, B. Schmid, J.R. Hutchinson, S.J. Shefelbine, Bonej: free and extensible bone image analysis in imagej, Bone 47 (6) (2010) 1076–1079.

[31] M. Kerschnitzki, P. Kollmannsberger, M. Burghammer, G.N. Duda, R. Weinkamer, W. Wagermaier, P. Fratzl, Architecture of the osteocyte network correlates with bone material quality, J. Bone Miner. Res. 28 (8) (2013) 1837–1845.

[32] L.-K. Huang, M.-J.J. Wang, Image thresholding by minimizing the measures of fuzziness, Pattern Recogn. 28 (1) (1995) 41–51.

[33] C.H. Li, P.K.S. Tam, An iterative algorithm for minimum cross entropy thresholding, Pattern Recogn. Lett. 19 (8) (1998) 771–776.

[34] T. Hildebrand, P. Rüegsegger, A new method for the model-independent assessment of thickness in three-dimensional images, J. Microsc. 185 (1) (1997) 67–75.

[35] R. Dougherty, K.-H. Kunzelmann, Computing local thickness of 3d structures with imagej, Microsc. Microanal. 13 (Supplement S02) (2007) 1678–1679.

[36] M. Albéric, M. Dean, A. Gourrier, W. Wagermaier, J.W.C. Dunlop, A. Staude, P. Fratzl, I. Reiche, Relation between the macroscopic pattern of elephant ivory and its three-dimensional micro-tubular network, PlosOne, in press.

[37] D.H. Pashley, Dentin a dynamic substrate – a review, Scanning Microsc. 3 (1) (1989) 161–174.

[38] Y.-C. Fung, Biomechanics: Mechanical Properties of Living Tissues, Springer, 2013.

[39] R. Wang, L. Addadi, S. Weiner, Design strategies of sea urchin teeth: structure, composition and micromechanical relations to function, Philos. Trans. R. Soc. Lond. B Biol. Sci. 352 (1352) (1997) 469–480.

[40] S.I. Kvaal, H.S. Koppang, T. Solheim, Relationship between age and deposit of peritubular dentine, Gerodontology 11 (2) (1994) 93–98.

[41] D. Arola, R.K. Reprogel, Effects of aging on the mechanical behavior of human dentin, Biomaterials 26 (18) (2005) 4051–4061.

[42] K.J. Koester, J.W. Ager, R.O. Ritchie, The effect of aging on crack-growth resistance and toughening mechanisms in human dentin, Biomaterials 29 (10) (2008) 1318–1328.

[43] G.R. Holland, The odontoblast process: form and function, J. Dent. Res. 64 (1985) 499–514.

[44] J. Camps, J.M. Saradell, J. Dejou, C. Pignoly, B. Jacquot, Influence of concentration and application time of maleic acid on dentin permeability, Dent. Mater. 11 (3) (1995) 177–181.